**PAPER** • **OPEN ACCESS**

# Propagation of vortex beams in atmospheric turbulence for uplink satellite links

To cite this article: Muhsin Caner Gökçe and Rudolf Saathof 2025 *Phys. Scr.* **100** 125211

Physica Scripta



OPEN ACCESS

RECEIVED
29 August 2025

REVISED
3 November 2025

ACCEPTED FOR PUBLICATION
25 November 2025

PUBLISHED
4 December 2025



PAPER

# Propagation of vortex beams in atmospheric turbulence for uplink satellite links

**Muhsin Caner Gökçe**[1,2,*] **and Rudolf Saathof**[1]

[1] Department of Space Systems Engineering, Delft University of Technology, 2629 HS Delft, The Netherlands
[2] Department of Electrical-Electronics Engineering, TED University, Çankaya, 06420 Ankara, Türkiye
[*] Author to whom any correspondence should be addressed.

**E-mail:** m.c.gokce@tudelft.nl, muhsin.gokce@tedu.edu.tr **and** r.saathof@tudelft.nl

**Keywords:** atmospheric turbulence, beam spread, scintillation index, strehl ratio, kurtosis, optical wave propagation, vortex beams

## Abstract

In this study, we examine the propagation characteristics of vortex-Gaussian beams in atmospheric turbulence for uplink free-space optical (FSO) links. Using the extended Huygens–Fresnel principles, we analytically derive key parameters, including the received intensity, second-order and fourth-order intensity moments, the Strehl ratio, the kurtosis parameter, and the effective beam spot radius. Then, we used phase-screen simulations to analyze the behavior of the scintillation index. Our findings demonstrate that vortex beams offer superior Strehl ratio performance compared to the Gaussian beam and exhibit greater resilience to atmospheric turbulence variations. Furthermore, the vortex beams exhibit kurtosis values below 3 and have a larger effective beam spot radius compared to Gaussian beams. Additionally, vortex beams exhibit a lower scintillation index compared to the Gaussian beam at longer propagation distances.

## 1. Introduction

Free-space optical (FSO) communication systems utilize laser beams to transmit large amounts of data between ground stations and satellites or other spacecraft [1, 2]. FSO communication offers several advantages over its radio frequency (RF) counterparts, including higher data rates, lower latency, smaller beam divergence, and reduced spectrum congestion, enabling transmission speeds of terabits per second. Additionally, FSO signals propagate with narrower beams than RF waves, minimizing signal loss and enhancing communication security. Unlike RF systems, FSO is not subject to spectrum allocation regulations. However, these systems are highly susceptible to atmospheric effects such as absorption and scattering, which reduce the signal's amplitude at the receiver [3]. Furthermore, atmospheric turbulence distorts the optical beam's wavefront, causing additional beam spreading [4], beam wander (movement around the receiver aperture) [5], and fluctuations in the received signal, known as scintillation [6].

Several effective techniques are available to mitigate the effects of turbulence on uplink beam propagation, including pre-correction adaptive optics [7–9], spatial diversity [10, 11], use of partially coherent beams [12], and beam shaping [13]. Each of these methods addresses atmospheric turbulence in distinct ways. For instance, pre-correction adaptive optics are applied at the ground terminal, using wavefront correction, measured on the downlink. Additionally, spatial diversity at both the transmitter and receiver provides statistically independent channels, helping reduce scintillation effects and increasing transmitted optical power. Using partially coherent beams also mitigates scintillation at the receiver but results in lower received power due to the inherent beam spreading.

In an FSO communication system, beam shaping plays a crucial role in controlling and modifying the properties of the optical beam, helping to reduce the impact of atmospheric turbulence and enhance overall system performance. Different types of laser beams, including flat-top beams, annular beams, multimode beams, and vortex beams, are employed to mitigate atmospheric turbulence. Among these, vortex beams are gaining increasing attention due to the distinct advantages they offer over other beam types. One significant

advantage is their ability to carry topological charge, which allows them to transmit information through their orbital angular momentum (OAM), thereby increasing the channel capacity. By utilizing OAM, multiple signals can be transmitted simultaneously within the same frequency band, boosting the total data capacity. Additionally, vortex beams are more resilient to atmospheric turbulence, making them particularly reliable for free-space optical communication systems. This resilience becomes more significant with higher topological charges. More specifically, vortex beams possess a helical phase front, and when viewed from the rear, their phase resembles a corkscrew. The corresponding intensity profile exhibits an annular (ring-shaped) structure, and as the topological charge increases, the central dark core of the beam expands. The topological charge defines the number of times the phase of light rotates around the beam's axis within one wavelength of propagation [14].

Horizontal propagation of vortex beams has been widely investigated, providing insight into their behavior in optical communication links [15–23]. For instance, Gbur and Tyson analyzed the changes in topological charge during propagation and suggested its potential as an information carrier in optical communications [15]. They also explored the critical distance for multiplexing using topological charge, noting that as the propagation distance increases, beam wander and spread lead to the beam's footprint exceeding the receiver aperture, making the detection of topological charge more difficult. Another notable study in this area is that Lukin *et al* [16] studied the beam spread of vortex beams in a turbulent atmosphere using numerical modeling, finding that vortex beams broaden less during propagation than Gaussian beams. Furthermore, two earlier studies focused on the effects of partial coherence on vortex beam propagation, in [17], an approximation for the cross-spectral density of the mutual coherence function of a partially coherent optical vortex field was presented. The propagation of partially coherent vortex beams in a turbulent atmosphere was addressed in [18], where the authors derived the intensity from the cross-spectral density function and found that the spreading of partially coherent vortex beams is less affected by atmospheric turbulence compared to partially coherent non-vortex beams. In a more recent study, the mutual coherence function of a vortex-Gaussian beam in atmospheric turbulence was reported for horizontal propagation [19], with the authors also examining the intensity and complex degree of coherence characteristics of vortex-Gaussian beams in turbulent conditions. Understanding the shape of a laser beam during propagation is important because it affects the characteristics of the transmitted beam, leading to performance variations. To analyze changes in beam quality, finding $M^2$ and kurtosis play an important role. In the literature, the analytical expression for the propagation factors ($M^2$-factors) and the Strehl ratio of vortex-Gaussian beams in non-Kolmogorov atmospheric turbulence is given in [20]. In addition, the investigation of the kurtosis parameter for vortex beams has also been reported in [21–23].

The design considerations for an OAM-multiplexed free-space data link were explored in [24]. The authors conducted simulations to analyze power loss, channel crosstalk, and power penalty for optical beams with OAM modes, focusing on scenarios with a limited-size receiver aperture. The authors in [25] present an adaptive MIMO FSO system that employs OAM multiplexing, leveraging spatial-mode multiplexing to enhance performance under atmospheric turbulence. Moreover [26], investigates the beam spreading and scintillation characteristics of a perfect vortex beam propagating through atmospheric turbulence using the multi-phase screen method. It is worth noting that the scintillation index of vortex beams has also been reported in earlier theoretical and experimental studies [27, 28]. In addition to existing FSO studies, an experimental study reported the intensity profiles of vortex beams in oceanic turbulence, using a spiral phase plate and a spatial light modulator, and the experimental results were also compared with theoretical predictions [29].

Two notable review articles have summarized the current understanding of vortex beam propagation [30, 31]. Soifer *et al* [30] provided an overview of vortex beam behavior in turbulent media, covering both integer and fractional vortex beams. Zhang *et al* [31] focused specifically on fractional vortex beams, which arise when the topological charge is non-integer; unlike integer-order vortex beams, these beams exhibit a phase discontinuity along the phase step, causing a disruption in the annular intensity ring during propagation.

Few studies have examined vortex beams for uplink communications. In [32], the bit-error-rate performance of vector vortex beams is discussed. In [33], the coherence analysis and the normalized average intensity distribution of Gaussian Schell-model vortex beams through slant atmospheric turbulence are presented. In [34], the authors examine the reliability of deep-space communication channels when utilizing OAM. They discuss the data rate and spectral efficiency of OAM states of single photon and highlight that, in the absence of an atmosphere, beam crosstalk is minimal. Their findings indicate that vortex beams offer superior spatial multiplexing capabilities, making them well-suited for high-capacity data transmission.

It is important to note that vortex beams exhibit a hollow center in their footprint under turbulence-free conditions. However, as the beam propagates through turbulence, its structure alters, and the central region becomes filled with intensity. This characteristic also makes vortex beams suitable for passive, cost-effective laser satellite communication systems that do not require adaptive optics.

It should be noted that the vortex-Gaussian beam analyzed in this work represents a special case of off-axis vortex beams. While the vortex-Gaussian beam has a phase singularity at its center, resulting in zero intensity along the axis, off-axis vortex beams shift the singularity away from the optical axis. This property can be

particularly useful when alignment with a detector is critical. In the literature, the propagation properties of the vortex beams have been reported in different turbulent medium such as free-space [35], atmospheric turbulence [36] and the oceanic turbulence [37, 38].

In this paper, we obtain closed-form analytical expressions for the average received intensity, Strehl ratio, kurtosis parameter, and effective beam spot radius using the extended Huygens–Fresnel principle for uplink laser satellite communications. The scintillation index is evaluated numerically using the phase-screen method, since obtaining an analytical solution through the Huygens–Fresnel principle is extremely challenging and would involve extensive derivations. The kurtosis parameter was evaluated using second-order and fourth-order intensity moments. To the best of our knowledge, the propagation characteristics of vortex–Gaussian beams for ground-to-satellite uplink communication have not been explored in detail. It should be note that vertical uplink scenario investigated in our work is fundamentally different than the horizontal link counterparts. This is due to the altitude-dependent vertical distribution of turbulence profiles and the associated long-distance propagation effects. Therefore, our study provides novel insights into vortex beam behavior under uplink conditions which cannot be directly extrapolated from horizontal studies and addresses a critical gap for practical applications for satellite communications. This work further provides a valuable framework for engineers designing next-generation laser satellite communication systems using vortex beams to enhance link quality.

## 2. Formulation

### 2.1. Optical intensity at the receiver plane

The source representation of a vortex-Gaussian beam can be described as [27, 28]

$$u(\mathbf{s}) = A \exp\left[-\frac{(s_x^2 + s_y^2)}{2\alpha_s^2}\right]\left[\frac{\sqrt{(s_x^2 + s_y^2)}}{\alpha_s}\right]^m \exp(jm\phi), \tag{1}$$

where $\mathbf{s} = (s_x, s_y)$ is the transmitter plane spatial coordinates, $A$ is the amplitude, $\alpha_s$ is the size of the Gaussian beam, $m$ is the topological charge, $j = \sqrt{-1}$, and $\phi = \arctan(s_y/s_x)$ is the azimuthal angle.

The Huygens–Fresnel principle can be applied to determine the intensity at the receiver plane

$$\begin{aligned}\langle I(\mathbf{p}, L)\rangle &= \langle u(\mathbf{p}, L)u^*(\mathbf{p}, L)\rangle \\ &= \frac{1}{(\lambda L)^2}\int_{-\infty}^{\infty}\int_{-\infty}^{\infty}\int_{-\infty}^{\infty}\int_{-\infty}^{\infty} \mathbf{d}^2\mathbf{s}_1\mathbf{d}^2\mathbf{s}_2 u(\mathbf{s}_1)u^*(\mathbf{s}_2) \\ &\quad \times \exp\left[\frac{jk}{2L}(|\mathbf{s}_1 - \mathbf{p}|^2 - |\mathbf{s}_2 - \mathbf{p}|^2)\right]\exp\left[-\frac{1}{2}D_\psi(\mathbf{s}_1, \mathbf{s}_2)\right],\end{aligned} \tag{2}$$

where $\mathbf{p} = (p_x, p_y)$ is the transverse plane receiver coordinates, i.e., observation point, $L$ is the propagation distance, $^*$ in the source term represents the complex conjugate, $k = 2\pi/\lambda$ in the propagation term is the wavenumber, $\lambda$ is the wavelength of the laser. The function $D_\psi$, which appears in the last line of equation (2), is the wave structure function, which describes the influence of turbulence and can be approximated as [39]

$$D_\psi(\mathbf{s}_1, \mathbf{s}_2) \cong \frac{2}{\rho_0^2}(s_1 - s_2)^2, \tag{3}$$

where $\rho_0$ represents the coherence length of a spherical wave traveling through a slant atmospheric path [40, 41]

$$\rho_0 = \left[1.457k^2\int_0^L C_n^2(h)dh\right]^{-3/5}, \tag{4}$$

where $h$ represents the distance parameter, $C_n^2(h)$ is the structure constant which depends on vertical height $h$. In the Hufnagel-Valley model, $C_n^2(h)$ is derived for the vertical path as [42]

$$\begin{aligned}C_n^2(h) &= 0.00594(w/27)^2(10^{-5}h)^{10}\exp(-h/1000) \\ &\quad + 2.7 \times 10^{-16}\exp(-h/1500) + C_{n0}^2\exp(-h/100),\end{aligned} \tag{5}$$

where $w$ represents the root mean square (RMS) wind speed, measured in (m/s), and $C_{n0}^2$ denotes the structure constant at ground level in $\mathrm{m}^{-2/3}$. The relation between the vertical path and slant paths is expressed as $h = \eta\cos(\zeta)$, where $\zeta$ denotes the zenith angle. By substituting this into equation (5), the Hufnagel-Valley model for $C_n^2(h)$ along the slant path is

$$C_n^2(\eta)=0.00594\left(\frac{w}{27}\right)^2(10^{-5}\eta\cos\zeta)^{10}\exp\left(-\frac{\eta\cos\zeta}{1000}\right)+2.7\times10^{-16}\exp\left(-\frac{\eta\cos\zeta}{1500}\right)+C_{n0}^2\exp\left(-\frac{\eta\cos\zeta}{100}\right). \quad (6)$$

In the framework of the extended Huygens–Fresnel principle, the receiver's field is derived as the convolution of the spherical wave response of the turbulent medium with the source field. Equation (2) is formulated based on the application of this principle, which explains why the spatial coherence length $\rho_0$ for a spherical wave is used in equation (2).

A direct solution for equation (2) cannot be obtained when equation (1) is used, unless the source is represented in terms of Hermite polynomials. To solve equation (2), the last two terms in equation (1) are rewritten in terms of Hermite polynomials, defined as [43]

$$\left[\frac{\sqrt{(s_x^2+s_y^2)}}{\alpha_s}\right]^m\exp(jm\phi)=\sum_{m_0=0}^{m}\frac{j^{m_0}}{(2\alpha_s)^m}\binom{m}{m_0}H_{m-m_0}(s_x)H_{m_0}(s_y), \quad (7)$$

where $H_m(.)$ denotes the Hermite polynomial of order $m$, and $\binom{m}{m_0}$ represents the binomial coefficient. By inserting equation (7) into equation (1), we rewrite the source field expression as

$$u(\mathbf{s})=A\exp\left[-\frac{(s_x^2+s_y^2)}{2\alpha_s^2}\right]\sum_{m_0=0}^{m}\frac{j^{m_0}}{(2\alpha_s)^m}\binom{m}{m_0}H_{m-m_0}(s_x)H_{m_0}(s_y). \quad (8)$$

By inserting equation (3) and equation (8) into equation (2) and solving it, we obtain the optical intensity of the vortex beams at the receiver plane as

$$\langle I(\mathbf{p},L)\rangle=\frac{A^2}{(\lambda L)^2}\sum_{m_0=0}^{m}\sum_{m_1=0}^{m}\frac{1}{(2\alpha_s)^{2m}}j^{m_0}(-j)^{m_1}\binom{m}{m_0}\binom{m}{m_1}I_xI_y, \quad (9)$$

where $I_x$ is defined as

$$\begin{aligned}I_x &= \pi\sum_{p=0}^{\frac{m-m_1}{2}}\sum_{k=0}^{m-m_1-2p}\sum_{q=0}^{\frac{m-m_0}{2}}\sum_{w=0}^{\frac{m-m_1-2p-k}{2}}\\ &\times(-1)^{3m-2m_1-p-k-m_0+w+q+1}2^{-\frac{m-m_1-2p}{2}}\\ &\times\frac{(m-m_1-2p)!}{(m-m_1-2p-k)!k!}\frac{(m-m_1)!}{(m-m_1-2p)!p!}\frac{(m-m_0)!}{(m-m_0-2q)!q!}\frac{(m-m_1-2p-k)!}{(m-m_1-2p-k-2w)!w!}\\ &\times\left(\frac{j}{\sqrt{C_1}}\right)^{1+m-m_1-2p}\exp\left(\frac{D_x^2}{4C_1}+\frac{G_x^2}{4K}\right)\left(\frac{j}{\sqrt{K}}\right)^{1+m-m_0+m-m_1-2p-k-2q-2w}\\ &\times\left(\frac{jE}{\sqrt{2C_1}}\right)^{m-m_1-2p-k-2w}H_k\left(\frac{jD_x}{\sqrt{2C_1}}\right)H_{m-m_0+m-m_1-2p-k-2q-2w}\left(\frac{jG_x}{2\sqrt{K}}\right),\end{aligned} \quad (10)$$

where $C_1=\frac{1}{2\alpha_s^2}+\frac{jk}{2L}+\frac{1}{\rho_0^2}$, $D_x=p_x\frac{jk}{L}$, $G_x=\frac{D_xE}{2C_1}-D_x$, $E=\frac{2}{\rho_0^2}$, $K=B_1-\frac{E^2}{4C_1}$, $B_1=\frac{1}{2\alpha_s^2}-\frac{jk}{2L}+\frac{1}{\rho_0^2}$. To derive $I_y$, replace $D_x$, $G_x$, $(m-m_0)$, and $(m-m_1)$ in equation (10) with $D_y$, $G_y$, $m_0$, and $m_1$, respectively. Afterward, substitute $p_x$ with $p_y$. In solving equation (9), we apply the integral expression we formulated in equation (A1) of Appendix A.

### 2.2. Strehl ratio

The Strehl ratio is a crucial parameter for evaluating the quality of an optical beam or imaging system. It compares the maximum intensity of an optical beam in turbulence to that in free space. Ranging from 0 to 1, a Strehl ratio close to 1 indicates high beam quality, while a lower value reflects aberrations due to atmospheric turbulence. The Strehl ratio is defined as

$$\mathrm{SR}=\frac{\langle I(\mathbf{p},L)\rangle_{\max}}{I^0(\mathbf{p},L)_{\max}}, \quad (11)$$

where $\langle I(\mathbf{p},L)\rangle_{\max}$ represents the maximum intensity in turbulence, and $I^0(\mathbf{p},L)_{\max}$ is the maximum intensity in the absence of turbulence.

### 2.3. Kurtosis parameter of vortex beams

The kurtosis parameter, representing the degree of sharpness or flatness of the beam profile during propagation, is expressed as the ratio between the fourth-order intensity moment and the square of the second-order intensity moment. For a specific transverse direction at the receiver, such as the $p_x$-axis, the kurtosis is defined in [44].

$$K_x = \frac{\langle p_x^4 \rangle}{\langle p_x^2 \rangle^2}, \tag{12}$$

where $\langle p_x^4 \rangle$ is the fourth-order intensity moment and $\langle p_x^2 \rangle$ is the second order intensity moment and $\langle p_x^r \rangle$ is evaluated by [45]

$$\langle p_x^r \rangle = \frac{\int_{-\infty}^{\infty}\int_{-\infty}^{\infty} p_x^r \langle I(\mathbf{p}, z = L)\rangle \, dp_x dp_y}{\int_{-\infty}^{\infty}\int_{-\infty}^{\infty} \langle I(\mathbf{p}, z = L)\rangle \, dp_x dp_y}, \quad r = 2, 4 \tag{13}$$

where denominator of equation (13) represents the total power at the receiver plane. It is important to note that $K_y$ is derived by replacing the coordinate parameter $p_x$ of the receiving plane with $p_y$ and $K_{xy} = (K_x K_y)^{1/2}$. By substituting the receiver plane intensity solution from equation (9) into the numerator of equation (13), we find

$$\int_{-\infty}^{\infty}\int_{-\infty}^{\infty} p_x^r \langle I(\mathbf{p}, z = L)\rangle \, dp_x \, dp_y = \frac{A^2}{(\lambda L)^2} \sum_{m_0=0}^{m}\sum_{m_1=0}^{m} \frac{1}{(2\alpha_s)^{2m}} j^{m_0}(-j)^{m_1} \times \binom{m}{m_0}\binom{m}{m_1} \int_{-\infty}^{\infty} p_x^r I_x \, dp_x \int_{-\infty}^{\infty} I_y \, dp_y. \tag{14}$$

By substituting $I_x$ and $I_y$ into equation (14) and performing the integration, we obtain analytical expressions for $\int_{-\infty}^{\infty} p_x^r I_x \, dp_x$ and $\int_{-\infty}^{\infty} I_y \, dp_y$, which are presented in equation (B1) and equation (B2) of Appendix B. Setting $r = 0$ in equation (14) results in the denominator of equation (13).

### 2.4. Effective beam spot radius

In atmospheric turbulence, a laser beam experiences greater spreading than in a free-space environment. Understanding beam spreading is crucial in uplink communication, as it influences the power loss at the detector and can also be used for the alignment purposes. The effective beam spot radius of a Gaussian-vortex beam can be described by [42]

$$\sigma_x^2 = \frac{2\int_{-\infty}^{\infty}\int_{-\infty}^{\infty} p_x^2 \langle I(\mathbf{p}, z = L)\rangle \, dp_x \, dp_y}{\int_{-\infty}^{\infty}\int_{-\infty}^{\infty} \langle I(\mathbf{p}, z = L)\rangle \, dp_x \, dp_y} = 2\langle p_x^2 \rangle. \tag{15}$$

where $\sigma_x$ shows the effective beam spot radius along the $p_x$ axis. The derivation steps of the second order intensity moment $\langle p_x^2 \rangle$ are reported in section 2.3. To compare the spreading of vortex beams with that of a Gaussian beam having the same source size at the transmitter, we investigate the spot radius ratio, which is

$$\text{Spot Radius Ratio} = \frac{\sigma_{x\_fs}}{\sigma_x} \tag{16}$$

where $\sigma_{x\_fs}$ shows the beam spot radius along the $p_x$ axis in the absence of turbulence. We perform this comparison to identify which beam undergoes less additional spreading in a vertical atmospheric turbulence link. In other words, we want to determine which beam is resilient to atmospheric turbulence. A similar comparison is presented by Andrews and Phillips on page 718 of [42], comparing Hermite-Gaussian beams with the Gaussian beam.

### 2.5. Scintillation index

Scintillation refers to the fluctuations in light intensity caused by turbulence in the medium through which a laser beam propagates. These fluctuations in the optical wave are quantified by the scintillation index. In this study, we employ the phase screen simulation method, since deriving an analytical solution using the Huygens–Fresnel principle is highly challenging and would involve lengthy derivations.

A wave optics numerical propagation simulation is defined in Matlab, using the on-axis split-step approach with the angular spectrum method [46]. Discretization over the boresight is done by assuming random phase screens at 9 altitudes $h$ using [47]:

$$h = \begin{bmatrix} 0 & 100 & 600 & 1250 & 2500 \\ 5800 & 10\cdot 10^3 & 20\cdot 10^3 & 40\cdot 10^3 & 70\cdot 10^3 \end{bmatrix} \text{m}. \tag{17}$$

The phase screens have an inner scale $l_0$ of 5 mm and an outer scale of 1000 m. The field has a diameter of 4 m and a pixel size of $256 \times 256$. Nine sub-harmonic layers have been used, to have a representative amount of angle of arrival fluctuations. To avoid frequency leakage, a windowing function has been used, that has a flat top in the dominant part of the phase screen. The edge consists of half a period of a cosine function, with a nominal width of 32 pixels. As the field is significantly larger than the dimensions of the optical beam, tip-tilt aberrations are sufficiently represented in the phase screens. The amplitude of the phase screens have been scaled using the partial Fried parameter:

$$r_{0,i} = \left[0.423k^2 \sec\zeta \int_{h_i}^{h_{i+1}} C_n^2(z)\,dz\right]^{-3/5}. \tag{18}$$

Note that the angular spectrum method is an exact wave propagation technique. However, at longer propagation distances, the field amplitude may extend beyond the simulation domain boundaries, leading to numerical errors due to the clipping of the electric field at the edges of the domain. To avoid this issue, the propagation from the upper atmosphere to the satellite is modeled using Fraunhofer propagation, which provides the electric field in the far field. This approximation is valid for distances greater than the Fraunhofer distance, $\frac{2D^2}{\lambda}$, which is 645 km for a beam width of 1 m. This condition is satisfied for satellites in low Earth orbit (LEO) with elevation angles up to 45°.

## 3. Numerical results

In this section, we examine the properties of vortex beams in atmospheric turbulence for uplink satellite communication links. The analysis focuses on the propagation of vortex beams with topological charges $m = 1$ and $m = 2$, while the $m = 0$ case corresponds to a Gaussian beam. The discussion includes an evaluation of the Strehl ratio (figures 1–3), the Kurtosis parameter (figures 4–6), the effective beam spot radius (figures 7–9), and the scintillation index (figure 10). The propagation characteristics of vortex beams are shown in all figures and compared with those of the Gaussian beam. All parameters are set to the values listed in table 1, unless otherwise specified in the figure captions or within the figures themselves.

It is noteworthy that the simulation scenario assumes a Low Earth Orbit satellite positioned at an altitude of $h = 500$ km with an elevation angle of $\zeta = 45°$. Note that the satellite's altitude is determined by multiplying the propagation distance by the cosine of the zenith angle $h = L\cos(\zeta)$. Furthermore, the ground-level transmitter utilizes vortex beams with a source size of $\alpha_s = 20$ cm and incorporates different topological charges ($m = 1$ and $m = 2$).

In figure 1(a), the Strehl ratio is plotted as a function of the propagation distance for both the vortex beams and the Gaussian beam in atmospheric turbulence for uplink satellite links. In figure 1(b), the Strehl ratio of the vortex beam with $m = 1$ is plotted for different ground-level structure constants. As seen in figure 1(a) that as the propagation distance increases the Strehl ratio decreases. At a propagation distance of $L = 707$ km, the Strehl ratios of the vortex beams are significantly higher than that of the Gaussian beam. Furthermore, the curves show a bump at various propagation distances for $m = 1$ and $m = 2$. These bumps may result from numerical inaccuracies in MATLAB's `max` function, which is unable to capture multiple maxima. The Strehl ratio decreases monotonically beyond $L = 300$ km. It is important to note that the boundary layer (0-2 km), also referred to as the surface layer, is the most influential region of atmospheric turbulence for optical wave propagation. In this region, strong winds and thermal gradients significantly impact the propagation of optical beams, causing wavefront deformations results in beam spread, beam wander and scintillation, which can notably affect laser communication links. The next atmospheric layer extends from 2 km up to 20 km and contributes to beam wander due to higher wind speeds and jet streams. After 20 km of propagation, the impact of turbulence on the optical beam becomes negligible [48]; however, diffraction of the optical beam continues until it reaches the destination point. As shown in figure 1(b), the Strehl ratio decreases as the ground-level structure constant increases, which is consistent with expectations.

In figure 2(a), we show the Strehl ratio as a function of the ground-level structure constant $C_{n0}^2$ for both vortex beams and the Gaussian beam. Compared to figure 2(b), we chose a longer propagation distance and a ground-level parameter set with lower $C_{n0}^2$ values. As observed in figure 2, the Strehl ratio decreases as $C_{n0}^2$ increases. However, with an increase in topological charge, the Strehl ratio starts to improve. From this, we can conclude that a vortex beam with a higher topological charge offers better Strehl ratio performance compared to the Gaussian beam and thus it is more beneficial to free-space optical communications. This can be physically attributed the phase of vortex beams, which may enhance their ability to resist the destructive effects of atmospheric turbulence compared to the Gaussian beam. Vortex beam imposes angular momentum on the beam, which changes how it interacts with turbulence. It is worth noting that the majority of turbulence layers are concentrated near the Earth's surface due to the presence of gases, molecules, suspended particles, and other factors. According to the Hufnagel-Valley model, the density of these atmospheric layers decreases with increasing height above the ground. As expressed in equation (4), the coherence length is derived by integrating the Hufnagel-Valley model over the propagation distance. Consequently, initializing the integral with the ground-level structure constant at the Earth's surface plays a crucial role in laser satellite communications. This is the reason why ground-level structure constant affects the Strehl ratio in figure 2. In figure 2(b), we used the same parameter set as in figure 2(a), but with a shorter propagation distance and higher ground-level $C_{n0}^2$ values. This illustrates that, despite the reduced propagation distance, the increase in the ground-level structure

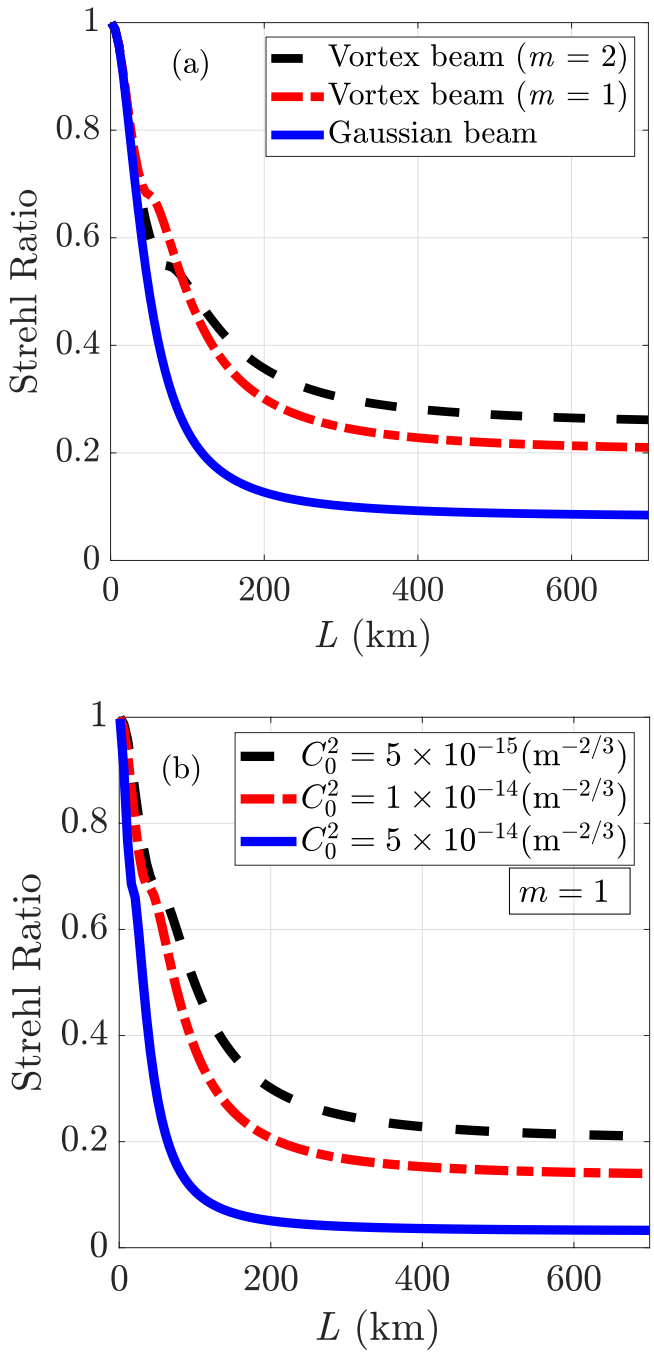


**Figure 1.** (a) Strehl ratio versus propagation distance $L$ for vortex and Gaussian beams. (b) Strehl ratio versus the propagation distance for various ground-level structure constants.

constant leads to a substantial decrease in the Strehl ratio, resulting in values lower than those shown in figure 2(a).

As shown in figure 3(a), we illustrate the impact of wind speed on the Strehl ratio for both vortex and Gaussian beams propagating in a vertical link in the presence of atmospheric turbulence, $C_{n0}^2 = 5 \times 10^{-15}$. It is seen that as the wind speed increases, the Strehl ratio decreases. The wind distorts the wavefronts of optical beams, leading to a reduction in beam intensity. However, as the topological charge increases, the optical beam becomes more resistant to atmospheric turbulence, resulting in a smaller reduction in peak intensity. This improved resilience under turbulence conditions leads to an increase in the Strehl ratio. In figure 3(b), the parameters are kept the same as in figure 3(a), except that the ground-level structure constant is increased to $C_{n0}^2 = 1 \times 10^{-13}$. As observed in the figure, this increase in the ground-level structure constant leads to a significant reduction in the Strehl ratio. Moreover, since the beams propagate through stronger turbulence, the Strehl ratio becomes less sensitive to changes in wind speed.

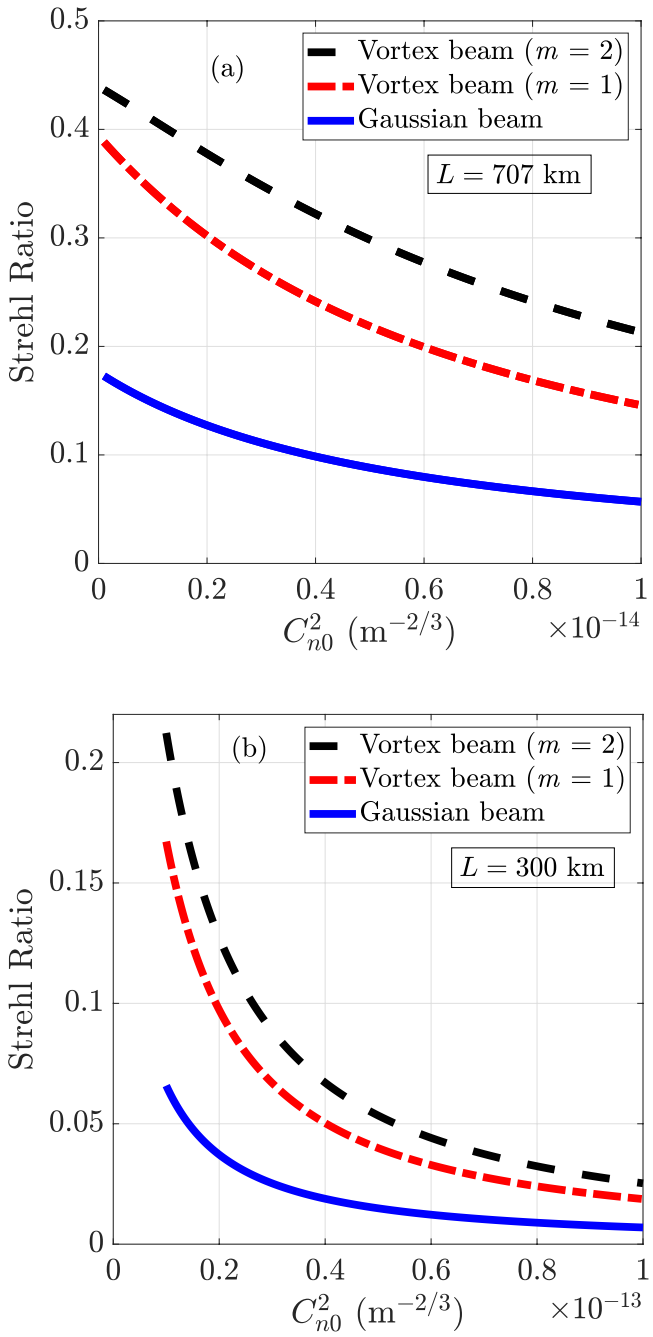


**Figure 2.** (a) Strehl ratio versus ground-level structure constant $C_{n0}^2$ for vortex and Gaussian beams at $L = 707$ km under relatively lower $C_{n0}^2$ values. (b) Strehl ratio versus ground-level structure constant $C_{n0}^2$ for vortex and Gaussian beams at $L = 300$ km under relatively higher $C_{n0}^2$ values.

Figure 4 illustrates the variations in the kurtosis parameter as a function of the propagation distance for both vortex beams and the Gaussian beam. For the Gaussian beam, the kurtosis parameter remains constant at a value of 3 throughout propagation, as expected [49, 50], due to its symmetric and self-similar intensity profile, which is referred to as Mesokurtic. In contrast, for vortex beams, the kurtosis parameter decreases with increasing topological charge. This occurs because higher topological charges cause the tail of the vortex beam to expand and exceed that of the Gaussian beam, resulting in a Platykurtic shape. Kurtosis is an effective measure of beam quality, reflecting how turbulence and propagation distance distort the beam. A vortex beam exhibiting a value close to 3 indicates that it has traveled a long distance through turbulence and evolved into a shape resembling a Gaussian beam.

In figure 5, the kurtosis parameter is shown as a function of the ground-level structure constant for both vortex beams and the Gaussian beam, with a propagation distance of $L = 707$ km. The results indicate that as the ground-level structure constant increases, the kurtosis parameter of the vortex beams also increases and eventually converges to the Gaussian beam limit, $K_x = 3$. At a fixed structure constant, the vortex beam with a

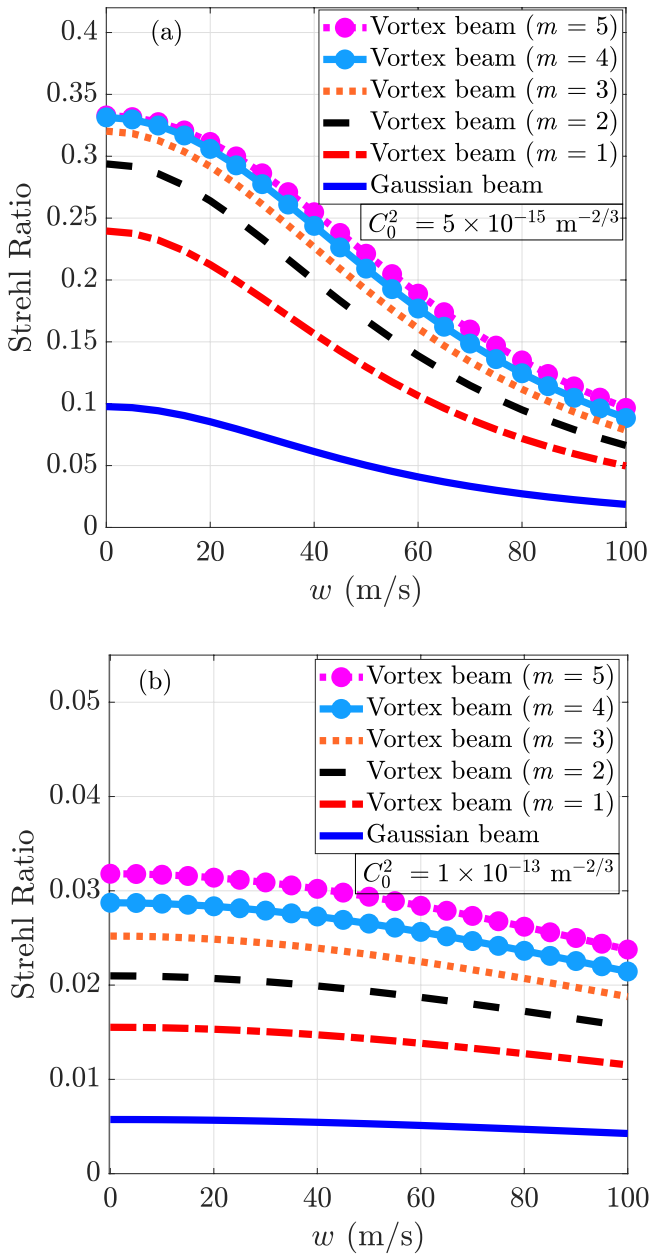


**Figure 3.** (a) Strehl ratio versus wind speed $w$ for vortex beams and a Gaussian beam, with a propagation distance of $L = 707$ km and a ground level structure constant of $C_{n0}^2 = 5 \times 10^{-15}$. (b) Strehl ratio versus wind speed $w$ for vortex beams and a Gaussian beam, with a propagation distance of $L = 707$ km and a ground level structure constant of $C_{n0}^2 = 1 \times 10^{-13}$.

topological charge of $m = 2$ is observed to have the lowest kurtosis parameter. Physically, this behavior can be explained as follows: in the absence of turbulence (i.e., for very low structure constants), the kurtosis parameter of the vortex beams approaches $K_x = 3$ due to the diffraction effects during long-distance propagation. However, when ground-level turbulence is strong (i.e., with a high structure constant), the vortex beams reach $K_x = 3$ more rapidly compared to cases with negligible turbulence. The distortions on the wavefront of the vortex beam originate at ground level and progressively intensify as the beam propagates toward the destination.

In figure 6, the kurtosis parameter is illustrated versus the zenith angle $\zeta^\circ$ for both vortex beams and the Gaussian beam, with a propagation distance of $L = 707$ km. When the zenith angle increases, kurtosis parameter of the vortex beams increases and eventually becomes $K_x = 3$ at highest value of the zenith angle. This indicates that vortex beams experience significant turbulence during horizontal propagation, causing the vortex laser to resemble the shape of a Gaussian distribution.

In figure 7, the variation of the beam spot radius with propagation distance is depicted for both vortex beams and the Gaussian beam. At any given propagation distance, the effective beam spot radius of vortex beams is larger than that of the Gaussian beam, and it increases further with higher topological charges. In

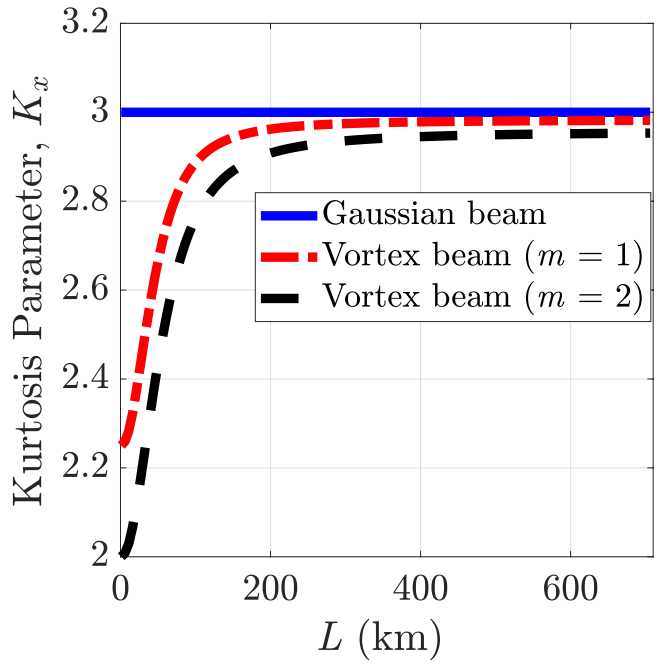


**Figure 4.** Kurtosis parameter, $K_x$, versus propagation distance, $L$, for vortex beams and the Gaussian beam.

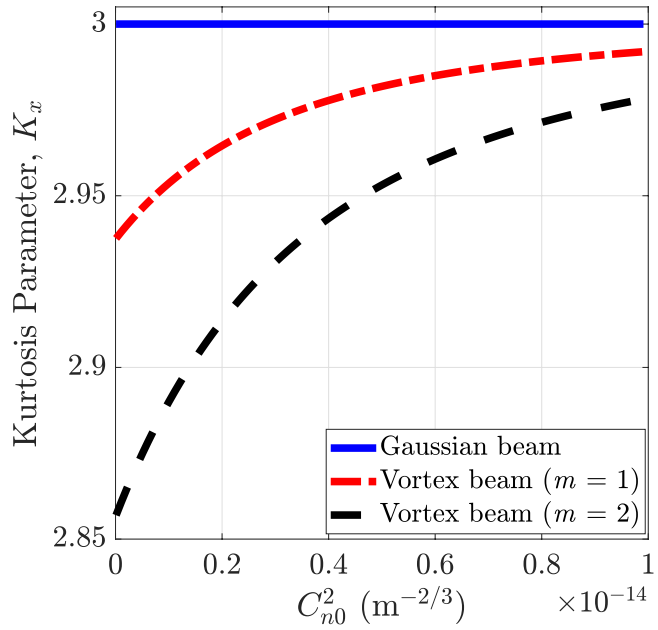


**Figure 5.** Kurtosis parameter, $K_x$, versus ground-level structure constant, $C_{n0}^2$, for vortex beams and the Gaussian beam, with a propagation distance of $L = 707$ km.

figure 8, the relationship between the effective beam spot radius and the source size is analyzed for both vortex beams and the Gaussian beam at $L = 707$ km. For small source sizes, vortex beams exhibit a much larger effective beam spot radius compared to the Gaussian beam. However, as the source size grows, the spot size difference between the two beam types gradually decreases. Additionally, the effective beam spot radius decreases for all beams as the source size increases. This trend is expected because a larger source size reduces the diffraction effect, leading to a smaller effective beam spot radius at $L = 707$ km.

Figure 9 employs the definition from equation (16) to illustrate the relationship between the spot radius ratio and propagation distance for vortex beams and the Gaussian beam. The figure reveals that the spot radius ratio decreases as the propagation distance increases, i.e., turbulence increases. The vortex beam with

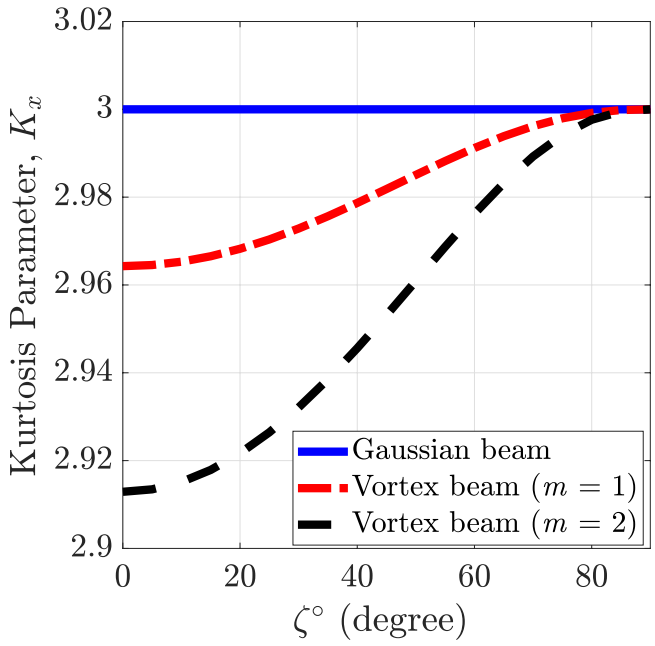


**Figure 6.** Kurtosis parameter, $K_x$, versus zenith angle, $\zeta^\circ$, for vortex beams and the Gaussian beam, with a propagation distance of $L = 707$ km.

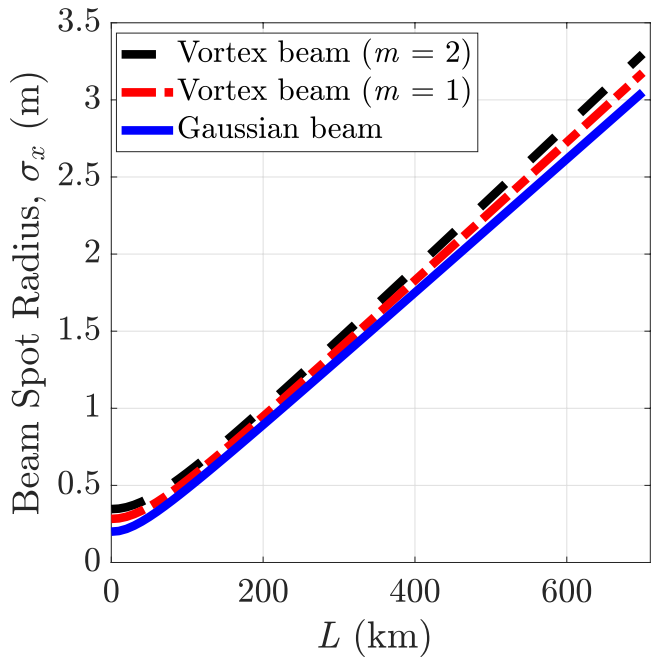


**Figure 7.** Effective beam spot radius, $\sigma_x$, versus propagation distance, $L$, for vortex beams and the Gaussian beam.

$m = 2$ has the greatest spot radius ratio. This ratio compares the effective beam size in free space to its size in turbulence. With increasing turbulence, the beam size becomes significantly larger than its size in free space, resulting in lower ratio values. The results suggest that vortex beams are more resistant to atmospheric turbulence compared to the Gaussian beam, and their resilience improves with higher topological charges. Since the vortex beam is less influenced by turbulence compared to the Gaussian beam.

Figure 10 shows the progression of the on axis scintillation index over increasing distance. Because of the limitations of phase screen propagation, we were only able to show the scintillation index up to 100 km, and at the far field, which we inferred to 707 km, to align with the other results. To improve the data points at the first 100 km, we made the x-axis logarithmic. The scintillation index of vortex beams initially is saturated, because of

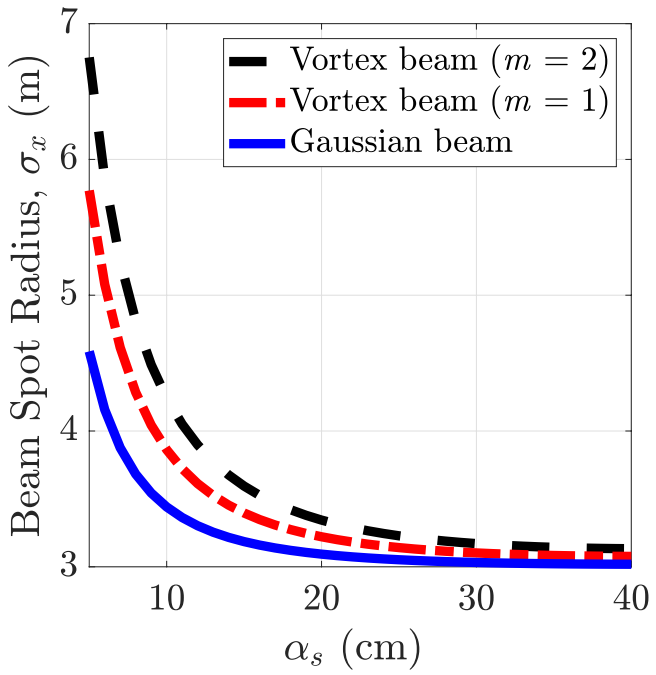


**Figure 8.** Effective beam spot radius, $\sigma_x$, versus source size, $\alpha_s$, for vortex beams and the Gaussian beam, with a propagation distance of $L = 707$ km.

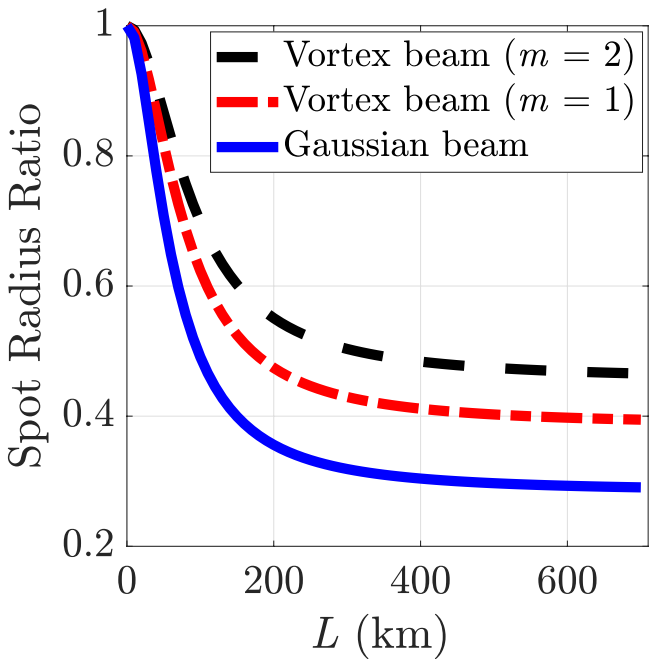


**Figure 9.** Ratio of spot radius in free space to spot radius in turbulence obtained for vortex beams and the Gaussian beam.

the lack of intensity in the center of the beam. This causes the minimum variation of optical power resulting in saturation of the scintillation index. At $L = 100$ km, the scintillation index of the vortex beams and the Gaussian beams are about equal. In the far field, the scintillation index of the Gaussian beam is 1.4 compared to 1.0 for vortex beams. This also shows that the vortex beams are more resilient to optical turbulence. The vortex beam maintains a zero-intensity center over considerable distances. As turbulence intensifies and begins to fill the beam's core with energy, the influence of the topological charge becomes pronounced. This phenomenon is especially noticeable in the far-field region.

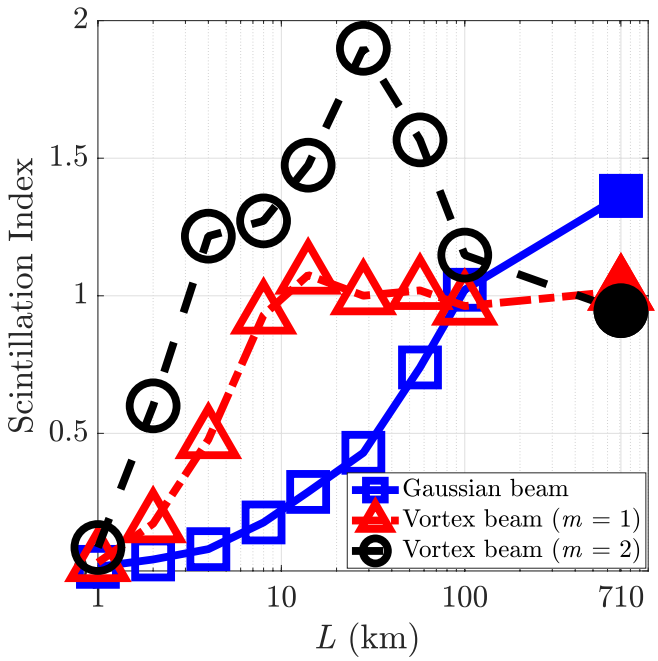


**Figure 10.** Scintillation index ratio versus propagation distance $L$ for vortex beams and the Gaussian beam. Active marked face colors provide the far field scintillation index. In the study, we assume the far field is at the propagation distance of $L = 707$ km.

**Table 1.** Fixed parameter values.

| Symbol | Definition | Value |
|---|---|---|
| $\lambda$ | Wavelength | 1550 nm |
| $C_{n0}^2$ | Ground-level structure constant | $5 \times 10^{-15}$ m$^{-2/3}$ |
| $w$ | Wind speed | 21 m/s |
| $\zeta$ | Zenith angle | 45° |
| $L$ | Propagation distance | 707 km |
| $\alpha_s$ | Source size | 20 cm |
| $m$ | Topological charge | 0, 1, 2 |
| $A$ | Amplitude of the optical field | 1 volt/m |

## 4. Discussion

In this study, we performed a preliminary analysis to assess whether uplink satellite communication quality can be improved. Our results indicate that replacing the existing Gaussian beam with vortex beams could enhance the system's resilience to atmospheric turbulence, leading to more stable communication between ground-level terminals and satellite links.

It is important to highlight that, due to long-distance optical wave propagation, both turbulence effects and the diffraction of the optical beam become significant. Consequently, the effective beam spot diameter, also referred to as the beam footprint diameter, reaches about 6 to 7 meters when the system parameters are set according to table 1. This large footprint makes it difficult for the receiver aperture to capture the full beam and fully exploit the multiplexing capabilities of vortex beams. Moreover, as the kurtosis of the vortex beams approaches 3, the beam shapes and phase patterns are distorted by atmospheric turbulence. Consequently, we can conclude that multiplexing using topological charge is more effective for shorter distances. Adaptive optics, a method to reduce the effects of turbulence, could enhance vortex beam propagation, and we will investigate this in our future study.

To the best of our knowledge, a closed-form expression for the scintillation index of a vortex-Gaussian beam has not been reported for uplink satellite links. In this study, to gain preliminary insight into the on-axis scintillation behavior of the vortex-Gaussian beam in uplinks, we employ the split-step phase screen method and compute scintillation index values for propagation distances up to 100 km. Due to the limitations of the phase screen method, we were unable to calculate the scintillation at $L = 707$ km. Instead, we evaluate both the Gaussian and vortex beams in the far field. The results demonstrate that the vortex beam exhibits better

scintillation performance compared to the Gaussian beam. Additionally, we note that up to 100 km, the vortex beam maintains its characteristic zero-intensity on-axis structure, leading to a higher scintillation index in this range.

Based on our findings, our future objective is to derive an analytical expression for the scintillation index of the vortex-Gaussian beam.

## 5. Conclusion

This study investigates the propagation properties of vortex beams in atmospheric turbulence for uplink communication links. Using the Huygens–Fresnel principle, we evaluate the average received intensity on the receiver plane. The Strehl ratio is then computed for both vortex and Gaussian beams. To calculate the Strehl ratio, the maximum intensity values from equation (9) are obtained using the `max(.)` function in MATLAB. We also compute the coherence length of the spherical wave, which is necessary for determining the received intensity through equation (9), by applying the Hufnagel-Valley model, which characterizes the vertical profile of atmospheric turbulence. Additionally, the second-order and fourth-order intensity moments of the optical beam are derived from the closed-form expression of intensity. Consequently, the kurtosis parameters for both Gaussian and vortex beams are calculated. The effective beam spot radius is evaluated using the second-order intensity moment. At last the scintillation index is determined using phase screen propagation.

In the study we have found that as the propagation distance, the ground level structure constant, wind speed increases the Strehl ratio decreases. However, an increase in the topological charge causes an increase in the Strehl ratio.

The kurtosis of a Gaussian beam is found to be 3, which is considered normal or mesokurtic, as it corresponds to the standard Gaussian distribution. This value serves as a reference for understanding how factors such as turbulence or diffraction may affect the statistical properties of vortex beams. In comparison, the kurtosis parameter of a vortex beam is generally less than 3, making it platykurtic, which implies that the tails of the vortex beam's intensity distribution are wider than those of the Gaussian beam. As the propagation distance, ground-level structure constant, and zenith angle increase, the kurtosis of vortex beams begins to rise, eventually approaching 3. In contrast, a rise in the topological charge leads to a decrease in kurtosis across all levels.

The effective beam spot size of the vortex beams are always larger than the Gaussian beam for the fixed source size. It is important to note that the vortex beam discussed here is composed of two components: the Gaussian beam and the vortex. Together, we refer to this as a vortex-Gaussian beam, and the source size mentioned pertains to the Gaussian beam component. The effective beam spot radius increases with increasing the propagation distance. At the propagation distance $L = 707$ km, an increase in the source size causes a decrease in the effective beam spot radius. For uplink satellite links, larger source sizes help reduce the diffraction effect and preserve transmitted power; however, they also make alignment more challenging. Further, we plotted the ratio of spot radius in free-space to spot radius in turbulence for vortex beams and the Gaussian beam. At last, we have compared the on-axis scintillation indices of the Vortex beams to the Gaussian beams. We showed that in the far field the scintillation index of vortex beams are lower.

This research offers valuable insights into the improved beam quality of vortex beams in atmospheric uplink propagation, with potential applications in laser satellite communication.

## Acknowledgments

This publication is part of the project DAILSCOM: Atmospheric Turbulence Informed Machine Learning for Laser Satellite Communications with file number 20617 of the research programme Open Technology Program 2023-2 which is (partly) financed by the Dutch Research Council (NWO).

## Data availability statement

All data that support the findings of this study are included within the article (and any supplementary files).

## Appendix A. Derivation for receiver intensity

To derive an analytical expression for the intensity at the receiver plane and resolve equation (2), we make use of the following integral formula we have developed

$$\int_{-\infty}^{\infty} dx\ H_y(ax)H_u(bx)\exp\left(-cx^2 \mp fx\right)$$
$$= (-1)^{u+y}(-j)\sqrt{\pi}\exp\left(\frac{f^2}{4c}\right)\sum_{q=0}^{y/2}\sum_{w=0}^{u/2}\frac{y!}{(y-2q)!\,q!}\frac{u!}{(u-2w)!\,w!}(-1)^{w+q}$$
$$\times\left(\frac{j}{\sqrt{c}}\right)^{1+y+u-2q-2w}a^{y-2q}b^{u-2w}H_{y+u-2q-2w}\left(\frac{jf}{2\sqrt{c}}\right). \tag{A1}$$

## Appendix B. Derivation for kurtosis parameter

By substituting $I_x$ from equation (10) into the integral in equation (14), $\int_{-\infty}^{\infty} p_x^r I_x\ dp_x$, and performing the integration, we obtain the analytical expression in equation (B1).

$$\int_{-\infty}^{\infty} p_x^r I_x dp_x = \pi\sqrt{\pi}\sum_{p=0}^{(m-m_1)/2}\sum_{k=0}^{(m-m_1-2p)}\sum_{q=0}^{(m-m_0)/2}\sum_{w=0}^{(m-m_1-2p-k)/2}\sum_{p_1=0}^{k/2}\sum_{p_2=0}^{(m-m_0+m-m_1-2p-k-2q-2w)/2}$$
$$\times 2^{-(m-m_1-2p)/2}(-1)^{(m-m_1+p)}2^{(k+m-m_0+m-m_1-2p-k-2q-2w-2p_1-2p_2)}$$
$$\times (2i)^{-(r+k+m-m_0+m-m_1-2p-k-2q-2w-2p_1-2p_2)}$$
$$\times (-1)^{(1+m-m_1-2p-k+m-m_0+w+q+p_1+p_2)}$$
$$\times \frac{(m-m_1-2p)!}{(m-m_1-2p-k)!k!}\frac{(m-m_1)!}{(m-m_1-2p)!p!}\frac{(m-m_0)!}{(m-m_0-2q)!q!}\left(\frac{j}{\sqrt{C_1}}\right)^{(1+m-m_1-2p)}$$
$$\times \frac{(m-m_1-2p-k)!}{(m-m_1-2p-k-2w)!w!}\frac{k!}{(k-2p_1)!p_1!}\left(\frac{j}{\sqrt{K}}\right)^{(1+m-m_0+m-m_1-2p-k-2q-2w)}$$
$$\times \left(\frac{jE}{\sqrt{2C_1}}\right)^{(m-m_1-2p-k-2w)}(-\varpi_3)^{(k-2p_1)}(-\varpi_4)^{(m-m_0+m-m_1-2p-k-2q-2w-2p_2)}$$
$$\times \frac{(m-m_0+m-m_1-2p-k-2q-2w)!}{(m-m_0+m-m_1-2p-k-2q-2w-2p_2)!p_2!}\left(\frac{1}{\sqrt{\varpi_1+\varpi_2}}\right)^{(P_\varpi)}$$
$$\times \mathrm{H}_{(r+k+m-m_0+m-m_1-2p-k-2q-2w-2p_1-2p_2)}(0). \tag{B1}$$

where $\varpi_1 = \left(\frac{k}{L}\right)^2\frac{1}{4C_1}$, $\varpi_2 = \left[\frac{k}{L}\left(\frac{E}{2C_1}-1\right)\right]^2\frac{1}{4K}$, $\varpi_3 = \frac{k}{L}\frac{1}{\sqrt{2C_1}}$, $\varpi_4 = \frac{k}{L}\left(\frac{E}{2C_1}-1\right)\frac{1}{2\sqrt{K}}$, $P_\varpi = 1+r+k+m-m_0+m-m_1-2p-k-2q-2w-2p_1-2p_2$.

Substituting $I_y$ into the integral in equation (14), $\int_{-\infty}^{\infty} I_y\ dp_y$, and performing the integration leads to the analytical expression in equation (B2).

$$\int_{-\infty}^{\infty} F_y dp_y = -j\pi\sqrt{\pi}\sum_{p=0}^{(m_1)/2}\sum_{k=0}^{(m_1-2p)}\sum_{q=0}^{(m_0)/2}\sum_{w=0}^{(m_1-2p-k)/2}\sum_{p_1=0}^{k/2}\sum_{p_2=0}^{(m_0+m_1-2p-k-2q-2w)/2}2^{-(m_1-2p)/2}$$
$$\times (-1)^{(1+m_0+2m_1-2p-k-2q-2w+k)}(-1)^{(m_1-2p-k+m_0)}(-1)^{w+q+p+p_1+p_2}$$
$$\times \frac{(m_1-2p)!}{(m_1-2p-k)!k!}\frac{(m_1)!}{(m_1-2p)!p!}\frac{(m_0)!}{(m_0-2q)!q!}\left(\frac{j}{\sqrt{C_1}}\right)^{(1+m_1-2p)}$$
$$\times \frac{(m_1-2p-k)!}{(m_1-2p-k-2w)!w!}\frac{k!}{(k-2p_1)!p_1!}\left(\frac{j}{\sqrt{K}}\right)^{(1+m_0+m_1-2p-k-2q-2w)}$$
$$\times \left(\frac{jE}{\sqrt{2C_1}}\right)^{(m_1-2p-k-2w)}\frac{(m_0+m_1-2p-k-2q-2w)!}{(m_0+m_1-2p-k-2q-2w-2p_2)!p_2!}$$
$$\times \left(\frac{j}{\sqrt{(\varpi_1+\varpi_2)}}\right)^{(1+k+m_0+m_1-2p-k-2q-2w-2p_1-2p_2)}(-\varpi_3)^{(k-2p_1)}$$
$$\times (-\varpi_4)^{(m_0+m_1-2p-k-2q-2w-2p_2)}\,\mathrm{H}_{(k+m_0+m_1-2p-k-2q-2w-2p_1-2p_2)}(0). \tag{B2}$$

## Author contributions

Muhsin Caner Gökçe 0000-0003-4465-1983
Conceptualization (equal), Formal analysis (equal), Investigation (equal), Methodology (lead), Visualization (equal), Writing – original draft (lead), Writing – review & editing (equal)

Rudolf Saathof 0000-0003-0368-0139
Conceptualization (equal), Formal analysis (equal), Investigation (equal), Project administration (lead), Visualization (equal), Writing – review & editing (equal)

## References

[1] Kaushal H and Kaddoum G 2016 Optical communication in space: challenges and mitigation techniques *IEEE Commun. Surv. Tutor.* **19** 57–96
[2] Majumdar A K 2005 Free-space laser communication performance in the atmospheric channel *J. Opt. Fiber Commun. Rep.* **2** 345–96
[3] Kaushal H, Jain V and Kar S 2017 *Free Space Optical Communication* vol 60 (Springer) (https://doi.org/10.1007/978-81-322-3691-7)
[4] Andrews L, Phillips R and Yu P 1995 Optical scintillations and fade statistics for a satellite-communication system *Appl. Opt.* **34** 7742–51
[5] Guo H, Luo B, Ren Y, Zhao S and Dang A 2010 Influence of beam wander on uplink of ground-to-satellite laser communication and optimization for transmitter beam radius *Opt. Lett.* **35** 1977–9
[6] Dios F, Rubio J A, Rodríguez A and Comeron A 2004 Scintillation and beam-wander analysis in an optical ground station-satellite uplink *Appl. Opt.* **43** 3866–73
[7] Leonhard N *et al* 2016 Real-time adaptive optics testbed to investigate point-ahead angle in pre-compensation of earth-to-GEO optical communication *Opt. Express* **24** 157–13
[8] Broekens K *et al* 2023 Field test demonstration of adaptive optics pre-correction for a terabit optical communication feeder link *IEEE International Conference on Space Optical Systems and Applications (ICSOS)* (IEEE) pp 175–81
[9] Broekens K *et al* 2023 Adaptive optics pre-correction demonstrator for terabit optical communication *International Conference on Space Optics—ICSO 2022* 12777 (SPIE) pp 758–66
[10] Reyes M, Comeron A, Alonso A, Rodriguez A, Rubio J A, Dios V F, Chueca S and Sodnik Z 2004 Ground-to-satellite bidirectional laser links for validation of atmospheric turbulence model *Free-Space Laser Communication and Active Laser Illumination III* vol 5160 (SPIE) pp 44–55
[11] Wu W-m, Ning Y, Zhang P-f, Feng X-x and Qiao C-h 2014 Scintillation analysis for multiple uplink gaussian beams in the presence of beam wander *Selected Papers from Conferences of the Photoelectronic Technology Committee of the Chinese Society of Astronautics: Optical Imaging, Remote Sensing, and Laser-Matter Interaction 2013* 9142 (SPIE) pp 580–5
[12] Wang M, Kane T, Yuan X, Zeng Y and Alharbi O 2018 Propagation of partially coherent beams with convex-shaped spatial coherence modulation in vertical turbulent links *Opt. Express* **26** 130–32
[13] Ata Y and Baykal Y 2015 Transmittance of multi gaussian optical beams for uplink applications in atmospheric turbulence *IEEE J. Sel. Areas Commun.* **33** 1996–2001
[14] Ke X and Wang J 2023 *Generation, Transmission, Detection, and Application of Vortex Beams* vol 447 (Springer) (https://doi.org/10.1007/978-981-99-0074-9)
[15] Gbur G and Tyson R K 2007 Vortex beam propagation through atmospheric turbulence and topological charge conservation *Journal of the Optical Society of America A* **25** 225–30
[16] Lukin V P, Konyaev P A and Sennikov V A 2012 Beam spreading of vortex beams propagating in turbulent atmosphere *Appl. Opt.* **51** C84–7
[17] Zhang Y, Tang M and Tao C 2005 Partially coherent vortex beams propagation in a turbulent atmosphere *Chinese Optics Letters* **3** 559–61
[18] Wang T, Pu J and Chen Z 2008 Propagation of partially coherent vortex beams in a turbulent atmosphere *Opt. Eng., Bellingham* **47** 002–36
[19] Gökçe M C, Baykal Y, Gerçekcioğlu H and Ata Y 2024 Intensity and degree of coherence of vortex beams in atmospheric turbulence *IEEE J. Quantum Electron.* **60** 6000208
[20] Li J, Wang W, Duan M and Wei J 2016 Influence of non-kolmogorov atmospheric turbulence on the beam quality of vortex beams *Opt. Express* **24** 413–20
[21] Zhou G 2014 Beam propagation factors and kurtosis parameters of a lorentz–gauss vortex beam *J. Opt. Soc. Am. A* **31** 1239–46
[22] Zhou G, Feng S, Xu Y and Zhou Y 2019 Beam propagation factor and kurtosis parameter of hollow vortex gaussian beams: an alternative method *J. Opt. Soc. Am. A* **36** 1908–16
[23] Hricha Z *et al* 2021 Parametric characterization of vortex cosine-hyperbolic-gaussian beams *Results in Optics* **5** 100120
[24] Xie G *et al* 2015 Performance metrics and design considerations for a free-space optical orbital-angular-momentum–multiplexed communication link *Optica* **2** 357–65
[25] Yousif B B and Elsayed E E 2019 Performance enhancement of an orbital-angular-momentum-multiplexed free-space optical link under atmospheric turbulence effects using spatial-mode multiplexing and hybrid diversity based on adaptive mimo equalization *IEEE Access* **7** 401–84
[26] Huang C, Bai L, Li J and Wang Y 2022 Beam spreading and scintillation of perfect vortex beam propagating in atmospheric turbulence *Thirteenth International Conference on Information Optics and Photonics (CIOP)* 12478 (SPIE) pp 582–6
[27] Chen Z, Li C, Ding P, Pu J and Zhao D 2012 Experimental investigation on the scintillation index of vortex beams propagating in simulated atmospheric turbulence *Appl. Phys. B* **107** 469–72
[28] Eyyuboğlu H T 2016 Scintillation behaviour of vortex beams in strong turbulence region *J. Mod. Opt.* **63** 2374–81
[29] Liu Z, Chen J and Zhao D 2017 Experimental study of propagation properties of vortex beams in oceanic turbulence *Appl. Opt.* **56** 3577–82
[30] Soifer V A, Korotkova O, Khonina S N and Shchepakina E A 2016 Vortex beams in turbulent media *Computer Optics* **40** 605–24
[31] Zhang H, Zeng J, Lu X, Wang Z, Zhao C and Cai Y 2022 Review on fractional vortex beam *Nanophotonics* **11** 241–73

[32] Cheng M, Dong K, Shi C, Mohammed A-A H T, Guo L, Yi X, Wang P and Li J 2022 Enhancing performance of air–ground oam communication system utilizing vector vortex beams in the atmosphere *Photonics* **10** 41 MDPI
[33] Li J, Zhang H and Lü B 2010 Partially coherent vortex beams propagating through slant atmospheric turbulence and coherence vortex evolution *Opt. Laser Technol.* **42** 428–33
[34] Wang X, Liu Y, Guo L and Li H 2014 Potential of vortex beams with orbital angular momentum modulation for deep-space optical communication *Opt. Eng., Bellingham* **53** 107–056
[35] Ma X, Wang G, Zhong H, Wang Y and Liu D 2021 The off-axis multi-gaussian schell-model hollow vortex beams propagation in free space and turbulent ocean *Optik* **228** 166180
[36] Wang Q, Zhang M, Zhang S and Qu J 2025 Propagation characteristics of partially coherent twisted off-axis double-vortex beams in atmospheric turbulence *Journal of the Optical Society of America A* **42** 276–84
[37] Chen D, Li J, Zhou Y and Dong K 2025 Propagation characteristics of off-axis laguerre–gaussian vortex beam in an oceanic turbulent stratified oblique channel *Appl. Opt.* **64** 8425–34
[38] Chen L, Wang G, Yin Y, Zhong H, Liu D and Wang Y 2023 Partially coherent off-axis double vortex beam and its properties in oceanic turbulence *Photonics* **11** 20 MDPI
[39] Baykal Y, Ata Y and Gökçe M C 2022 Underwater turbulence, its effects on optical wireless communication and imaging: a review *Opt. Laser Technol.* **156** 108624
[40] Baykal Y 2013 Coherence length in non-kolmogorov satellite links *Opt. Commun.* **308** 105–8
[41] Beland R R 1995 Some aspects of propagation through weak isotropic nonkolmogorov turbulence *Beam Control, Diagnostics, Standards, and Propagation* 2375 (SPIE) pp 6–16
[42] Andrews L C and Phillips R L 2005 *Laser Beam Propagation Through Random Media* 2nd edn (SPIE Press) (https://doi.org/10.1117/3.626196)
[43] Kimel I and Elias L R 1993 Relations between hermite and laguerre gaussian modes *IEEE J. Quantum Electron.* **29** 2562–7
[44] Martinez-Herrero R, Piquero G and Mejias P 1995 On the propagation of the kurtosis parameter of general beams *Opt. Commun.* **115** 225–32
[45] Gökçe M C, Baykal Y, Ata Y and Gerçekcioğlu H 2024 Multimode beam propagation through atmospheric turbulence *J. Quant. Spectrosc. Radiat. Transfer* **314** 108857
[46] Schmidt J D 2010 *Numerical Simulation of Optical Wave Propagation with Examples in MATLAB* (SPIE)
[47] Charnotskii M 2020 Comparison of four techniques for turbulent phase screens simulation *J. Opt. Soc. Am. A* **37** 738–47
[48] Quatresooz F and Oestges C 2025 $C^2$ modeling for free-space optical communications: a review *IEEE Access* **13** 279–21
[49] Luo S and Lü B 2002 Propagation of the kurtosis parameter of hermite-cosh-gaussian beams *Optik* **113** 329–32
[50] Lü B and Luo S 2002 Analytical expression for the kurtosis parameter of flattened gaussian beams propagating through abcd optical systems *J. Mod. Opt.* **49** 1731–8